Guiding Light in Monolayers of Sparse and Random Plasmonic Meta-atoms

Marinus A. Otte, M.-Carmen Estévez, David Regatos, Laura M. Lechuga, and Borja Sepúlveda*

Nanobiosensors and Bioanalytical Applications Group, Research Center on Nanoscience and Nanotechnology (CSIC) & CIBER-BBN, 08193 Bellaterra, Barcelona, Spain

The ability of surface plasmons to confine and transport electromagnetic (EM) energy has boosted the development of integrated nanophotonic circuitry combining subwavelength EM field localization and moderate propagation distances. When using thin metal films or stripes as waveguides, a trade-off between confinement and propagation is necessary. Whereas short-range surface plasmon polaritons (SPPs) offer strong confinement, their propagation distance is strongly suppressed by inherent ohmic losses.[1,2] On the contrary, long-range SPPs exhibit propagation distances longer than one centimeter in the infrared at the cost of poor spatial mode localization.[3−5] To tackle this trade-off, other waveguiding schemes have been proposed, such as metal—insulator—metal-,[6] hybrid-,[7,8] and channel waveguides,[9] offering both low propagation losses and strong mode confinement up to telecommunication frequencies. To achieve additional mode confinement and miniaturization, an alternative approach for nanoplasmonic waveguiding is offered by ordered arrays of metal nanoparticles. For interparticle separation distances lower than the size of the nanostructures, near-field optical coupling assures interparticle energy transfer with EM confinement well below the diffraction-limit. Following this path, linear chains of ordered nanoparticles have indeed proven their potential as nanoplasmonic waveguides.[10] Extension of these linear chains into two-dimensional arrays of metal nanostructures revealed the existence of in-plane plasmon modes based on either near-field interactions or diffractive far-field effects,[11−17] and out-of-plane subradiant lattice modes.[18] However, in all these cases the necessity of short interparticle distances and/or precise particle ordering puts serious demands on the employed fabrication techniques, typically requiring expensive methods that inhibit the patterning of large surface areas.

ABSTRACT Encouraged by the capacity of surface plasmons to confine and propagate electromagnetic fields, waveguiding concepts have been developed, including combinations of continuous metal films or ordered arrays of metal nanoparticles. So far, waveguiding in the latter systems has been based on near-field or diffractive coupling. Herein, we show that monolayers of sparse and disordered gold nanoparticles support a novel transverse-electric guided mode that, contrary to previous work, relies on the strong enhancement of the polarizability upon excitation of the nanoparticle LSPR, creating an effective refractive index sufficiently high to support light guidance over a large range of frequencies. Excitation of this guided mode offers interesting nanophotonics features and applications such as a tunable total absorption spectral band, attractive for light harvesting applications, or the generation of a large amplification of the sensitivity to changes of refractive index accompanied with striking enhancement of the limit of detection in real biosensing experiments.

KEYWORDS: nanoplasmonic waveguide · light-harvesting · label-free biosensing · gold nanodisks · optical biosensor

Herein, we report on a novel type of in-plane guided mode present in extremely thin monolayers of sparse and randomly distributed plasmonic nanoparticles. Compared to previous works, due to the large interparticle distances and their random distribution, no near-field or diffractive effects lie on the basis of this waveguiding behavior. Instead, these guided modes arise as a consequence of the large enhancement of the effective refractive index (RI) of the monolayer, thus creating an effective medium of plasmonic meta-atoms with large polarizability. Excitation of these guided modes in total internal reflection (TIR) can drastically increase light/matter interaction leading to interesting effects such as tunable total absorption of the incident photons with an extremely low quantity of plasmonic material, or large amplification of the sensitivity and limits of detection in biosensing measurements. The interest of these applications is boosted by the possibility to fabricate the random plasmonic monolayers with robust, low-cost, and wafer-scale self-assembled colloidal lithography techniques.[19]

THEORETICAL ANALYSIS

The waveguiding properties 2D nanoparticle arrays can be modeled by different theoretical models, among which those based on generalized sheet transition conditions (GSTC)[20] or dipolar approximations can be highlighted.[21] However, in this work the optical properties of a random and sparse distribution of subwavelength-sized nanoparticles are accurately described by the Maxwell–Garnett (MG) effective medium theory, in which the inhomogeneous medium is treated as a homogeneous medium with an effective refractive index. This approach is justified given the very low density of nanodisks to neglect near-field interactions. We model these disk-shaped nanostructures as infinitely small gold oblate ellipsoidal geometries, with a 1:5 aspect ratio between the short and long axis, respectively, being buried in a homogeneous dielectric ($n = 1.33$), as shown in Figure 1a. The shape anisotropy of the nanoparticles creates an effective optical birefringence and, therefore, distinction has to be made between the in- and out-of-plane effective refractive index ($n_{eff} = \eta + i\kappa$). Figure 1b shows the calculated real (η_{in}) and imaginary part (κ_{in}) of the in-plane n_{eff} of the anisotropic medium for different nanoellipsoid surface densities (F) as a function of the wavelength. The spectra exhibit a typical resonance shape with a large increase of η_{in} and κ_{in} near the localized surface plasmon resonance (LSPR) of a single ellipsoid ($\lambda_{LSPR} \approx 660$ nm). Over the entire analyzed wavelength range, higher disk densities are accompanied by higher values of η_{in} and κ_{in}. For volume concentrations as low as 6%, the effective RI in the vicinity of the resonance is already substantially larger than that of any material in nature. In contrast, the out-of-plane n_{eff} reveals much smaller values of η_{out} and κ_{out} with a blue-shifted peak, consequence of the weak polarizability of the ellipsoids in this direction (Figure 1c). Such behavior unambiguously shows the fundamental role that the LSPR plays in the optical properties of the effective medium.

The large enhancement of n_{eff} suggests the ability of these effective medium layers to act like nanophotonic waveguides, as long as the refractive index of the effective layer is larger than that of its cladding layers. This requirement is easily met for $\lambda \geq 650$ nm and $F \geq 2\%$, assuming the effective medium to be confined between glass ($n = 1.52$) and water ($n = 1.33$). To confirm the capacity of the effective media to support guided waves, wavelength-dependent mode solutions are calculated for different polarizations via a transfer matrix formalism valid for arbitrary anisotropic multilayers.[22,23] To model a nanoplasmonic waveguide we assume that the thickness of the monolayer is only 20 nm, comprised between two cladding layers (glass, $n = 1.52$ and water, $n = 1.33$). The chosen layer thickness of 20 nm, together with the imposed aspect

ratio of 5:1, therefore inherently results in nanoellipsoid diameters of 100 nm. The low values of η_{out} and κ_{out} rule out the existence of transversal magnetic (TM) modes; however, the transversal electric (TE) polarization only depends on η_{in} and κ_{in}, which are both greatly amplified near the resonance. As a consequence, guided mode solutions and their associated dispersion relation can be found for TE polarization when $F \geq 2\%$, as shown by the solid lines in Figure 1d.

For low concentrations ($F \approx 2\%$) the guided mode is restricted to a very short energy range. Because of the overall increase of n_{eff} for larger nanoellipsoid densities, the dispersion curves nicely illustrate that denser nanoparticle layers are expected to sustain waveguiding behavior over a longer energy range. The dispersion relations exhibit a region of anomalous dispersion ($dE/dk_\parallel < 0$ and $dn/d\lambda > 0$) in the high energy range, typically characterized by quasi-bound, leaky modes. This region transitions into a regime of normal dispersion ($dE/dk_\parallel > 0$ and $dn/d\lambda < 0$) showing large wave-vector values ($k_\parallel$) near the resonance energy of the single ellipsoids. In these regions, κ_{in} is greatly amplified (Figure 1b), yielding strong damping and hence very short propagation distance (Figure 1e). However, at lower energies (E < 1.77 eV, λ > 700 nm) guided modes with propagation distances larger than 100 μm can be achieved, owing to the drastic reduction of κ_{in} while keeping large values of η_{in}. For all concentrations there is a cutoff energy below which the guided mode is transformed into a leaky mode that is radiated toward the high RI substrate. Interestingly, near the cutoff energy the dispersion relation lies within the glass light cone, suggesting the possibility of excitation via prism-coupling in TIR. It should be noted that for effective medium layers thinner than 20 nm, the mode solutions are restricted to narrower energy ranges at similar volume concentrations of nanoparticles (Supporting Information, Figure S1). In contrast, thicker layers impose larger wavevectors of the supported guided modes, which restricts the prism coupling excitation to incidence angles very close to 90°. As a consequence, we have chosen the layer thickness to be 20 nm, assuring both strong dispersion and the possibility of prism-coupled excitation at lower incidence angles (70−80°). This selection will also allow the experimental verification with monolayers of nanoparticles with low volume to minimize their scattering cross section and dephasing effects. This excitation mechanism is demonstrated in Figure 2a and 2c, where the angle-dependent TE reflectivity spectra are calculated for $F = 2\%$ and $F = 8\%$, respectively. The latter is done for a prism-coupled Kretschmann configuration,[24] employing a transfer matrix formalism.[25] In both cases, reflectivity spectra exhibit a transition from a shallow peak at low incidence angle to a pronounced dip above TIR ($\theta_{TIR} > 61°$). Below this critical angle, a stationary resonance is expected at $\lambda \approx 660$ nm (E ≈ 1.87 eV),
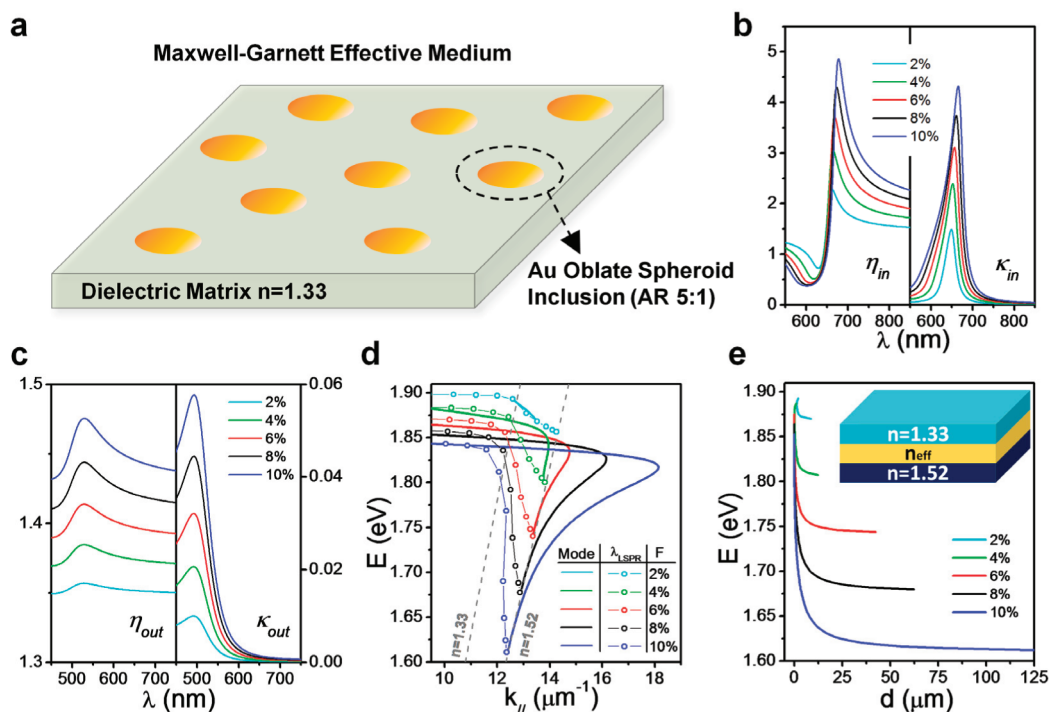
Figure 1. Calculated optical properties corresponding to monolayers of sparse and randomly ordered arrays of gold nanoellipsoids for different nanoparticle densities (F = 2−10%). (a) Schematics of the modeled Maxwell−Garnett effective medium, showing gold oblate spheroids in an otherwise homogeneous dielectric layer (n = 1.33) (b) Real η_{in} and imaginary part κ_{in} of the of the in-plane and (c) out-of-plane refractive indices as a function of the wavelength λ. (d) TE-guided mode dispersion curves (straight lines) and spectral resonance positions of angle-dependent reflectivity spectra (dash-dotted lines). (e) Propagation distances d of the TE-guided modes as a function of the mode energy E, together with waveguide schematics (inset).

corresponding to the resonance of a single nanoellipsoid excited along its long axis. However, when θ_{TIR} is surpassed, the observed dip is shifted toward higher wavelengths, showing strong dispersion. In agreement with the dispersion curves of Figure 1d this phenomenon is more pronounced for F = 8%, resulting in a total red-shift of 75 nm at θ = 85°. As expected, this strong dispersion is not observed when TM excitation is used (Supporting Information, Figure S2).

Such drastic changes in the TE reflectivity spectra already suggest the existence and possibility of excitation of a guided mode. However, this effect can be unambiguously shown depicting the resonance energies of the reflectivity spectra in Figure 1d (dash−dotted curves). Although the high-$k_{\parallel}$ region is inaccessible via TIR, the energy position of the reflectivity dips can match the dispersion relation of the guided mode in the vicinity of the cutoff energy for all nanoellipsoid concentrations (F = 2−10%). Only at this point, the phase matching condition is fulfilled and 100% of the energy is transferred to the guided mode. The latter is clearly illustrated in Figure 2 panels a and c, where the dark blue areas in the TIR region correspond to reflectivity values close to 0%. For low concentrations this phase matching occurs at θ = 70° at a wavelength that is slightly red-shifted compared to the LSPR of a single ellipsoid. In contrast, the dispersion

relation at higher concentrations imposes larger incidence angles and substantially longer wavelengths to satisfy the phase matching condition, thus explaining the strong red-shift of the reflectivity dip for F = 8% (θ = 85°). Note that for angles other than those corresponding to perfect light coupling, wave excitation is still possible, but the latter will occur less efficiently, resulting in less pronounced resonance reflectivity dips. The graphs in Figure 2b and 2d exemplify the extraordinary coupling of light into the guided modes, and moreover show that by using the incidence angle as a variable, the optical behavior of the effective medium can be tuned from that of an homogeneous ensemble of isolated nanoparticles, dominated by their LSPR, into a nanoplasmonic waveguiding medium characterized by extremely high levels of light absorption. This expected extraordinary degree of light uptake is unprecedented, especially considering the random ordering, low surface density, and the limited thickness (20 nm) of the modeled effective medium. In analogy, complete light absorption can also be achieved with SPPs that propagate along a planar 50 nm gold film.[26] Given the low nanoellipsoid densities (F = 2−10%) needed to achieve the same result, it becomes apparent that this effective medium requires up to 125 times less plasmonic material to absorb the same amount of light. Indeed, even for very low particle densities
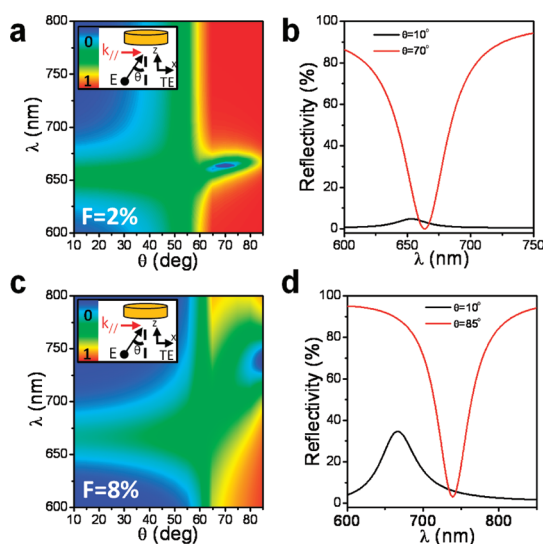
Figure 2. Calculated reflectivity spectra corresponding to monolayers of sparse and randomly ordered arrays of gold nanoellipsoid for $F = 2\%$ and $F = 8\%$. (a) TE reflectivity spectra for $F = 2\%$ as a function of the incidence angle θ and the wavelength λ. (b) Reflectivity spectra corresponding to $\theta = 10°$ and $\theta = 70°$ for $F = 2\%$, depicting the reflectivity as a function of the wavelength λ. (c) TE reflectivity spectra for $F = 8\%$ as a function of the incidence angle θ and the wavelength λ. (d) Reflectivity spectra corresponding to $\theta = 10°$ and $\theta = 85°$ for $F = 8\%$, depicting the reflectivity as a function of the wavelength λ.

($F = 2\%$) the absorbance of the plasmonic monolayer can be amplified from 20% at normal incidence to total absorption at $\theta = 70°$ incidence, which combined with very short mode propagation makes these effective layers very suitable as light harvesting devices. Energy harvesting generally aims for heat generation *via* nanoscale energy confinement, requiring the employed plasmonic structures to be tunable over a broad spectral range, thereby maintaining their light absorption efficiency.[27] Interestingly, the total absorption band can be tuned over the entire visible and NIR spectral ranges by changing the aspect ratio (Supporting Information, Figure S3), density, or composition of the employed nanoellipsoids, as well as the external RI.

Another effect that highlights the drastic change of the optical properties when the guided mode is excited is the sensitivity of the nanoplasmonic effective media to the refractive index changes of the external medium (Figure 3a), which constitutes the well-known basis of biosensing applications.[28−30] Below the critical angle, the sensitivity to the changes of refractive index ($\eta_B = \Delta\lambda_{LSPR}/\Delta n$) exactly fits the sensitivity of a single nanoellipsoid ($\eta_B \approx 275$ nm RIU^{-1}),[31] which is in agreement with the localized nature of the resonance in this regime. Most interestingly, once the waveguiding behavior sets in, η_B increases in a drastic manner. Clearly, this sensitivity enhancement is more pronounced for larger particle densities, surpassing 900 nm RIU^{-1} for $F = 10\%$ at $\theta = 85°$, implying a more
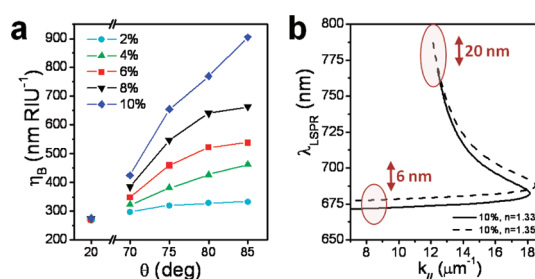

Figure 3. Theoretical bulk sensitivity analysis for monolayers of sparse and randomly ordered arrays of gold nanoellipsoids ($F = 2-10\%$). (a) Bulk sensitivities η_B calculated for $F = 2-10\%$ as a function of the incidence angle θ. (b) Calculated spectral mode dispersion curves ($F = 8\%$), depicting the resonance wavelength λ_{LSPR} as a function of the wave-vector $k_{\|}$ for bulk dielectric environments given by $n = 1.33$ (straight line) and $n = 1.35$ (dashed line).

than 3-fold amplification of η_B with respect to isolated nanoellipsoids. Such sensitivity amplification is a clear sign of the waveguiding behavior, as can be deduced from the variation of the dispersion relation of the guided mode under a RI change (Figure 3b). Near the LSPR wavelength the RI change induces a red-shift of the dispersion relation equal to that of the single nanoellipsoid ($\Delta\lambda_{LSPR} = 6$ nm), reflecting the localized nature of the excitation. In contrast, close to the cutoff wavelength, where the guided mode can be excited perfectly, the change in the dispersion relation generates a red-shift which is more than three times larger than the LSPR shift, thus explaining the drastic sensitivity enhancement upon mode excitation. Next to such valuable amplification of η_B, the extremely pronounced dips achieved when the phase matching condition is fulfilled also have striking effects on the signal-to-noise ratio of biosensing measurements, even with very low density of plasmonic nanoparticles, as will be demonstrated below.

EXPERIMENTAL RESULTS

To experimentally verify these theoretical predictions, short-ordered arrays of gold nanodisks (diameter $D = 100$ nm, height $H = 20$ nm) were prepared on glass substrates by hole-mask colloidal lithography,[19] allowing the fabrication of random distributions of metal nanodisks with tunable density. Figure 4 panels a and b represent the experimental TE reflectivity spectra as a function of θ of two monolayers with different density ($F \approx 5\%$ (A) and $F \approx 7.5\%$ (B)), clearly exemplifying all predicted signatures related to the excitation of a guided mode. First, the shallow reflectivity peaks located at $\lambda_{LSPR} \approx 710$ nm below the critical angle, which correspond to the resonance wavelength of a single nanodisk seating on glass, are transformed into profound dips in TIR. This transformation is accompanied by a substantial red-shift of the dip position for increasing incidence angles ($\Delta\lambda_{LSPR} \approx 44$ nm (A) and $\Delta\lambda_{LSPR} \approx 87$ nm (B) at $\theta = 85°$). This dispersion is depicted in Figure 4c in energy-scale, where the
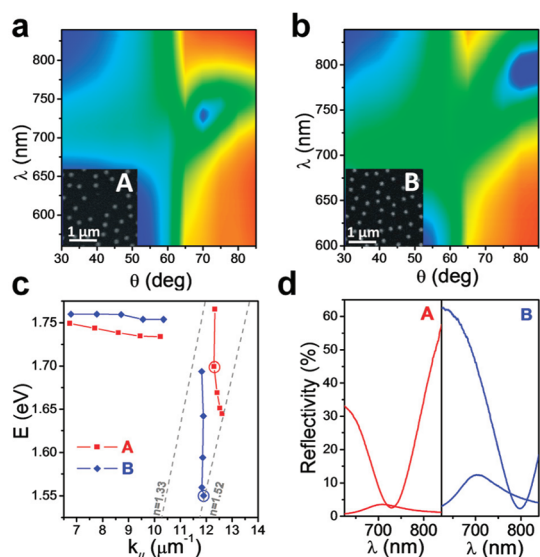
Figure 4. Experimental dispersion relations corresponding to sparse nanodisk arrays with disk densities given by $F \approx$ 5% (A) and $F \approx$ 7.5% (B). (a) TE reflectivity spectra showing the reflectivity as a function of the incidence angle θ and the wavelength λ, together with SEM image (inset) for nanodisk sample A and (b) sample B. (c) Experimental dispersion relations corresponding to the reflectivity spectra of samples A and B, depicting the resonance energy E as a function of the wave-vector $k_{\parallel}$. (d) Dip-shaped reflectivity spectra upon perfect mode excitation for sample A ($\theta = 70°$) and B ($\theta = 85°$), together with their peak-shaped spectral response obtained at $\theta = 30°$.

encircled points correspond to spectra where the phase matching condition is satisfied, resulting in almost zero reflection. Since the amount of scattered light trespassing the nanodisk arrays is extremely small compared to the light used for mode excitation (Supporting Information, Figure S4), it is safe to state that almost all in-coupled light is harvested by these nanostructured layers, yielding absorbance coefficients of approximately 96%–97% (Figure 4d). Note that all the experimental results are red-shifted with respect to the theoretical predictions due to near-field interaction of the nanodisks with the substrate, which is not taken into account in the MG formalism. On the other hand, no dispersion is observed for the TM polarization (Supporting Information, Figure S5), as a consequence of the expected absence of available guided modes. Conclusively, this observed spectral behavior undisputedly shows the different response exhibited by the nanodisks depending on the excitation conditions.

The waveguiding behavior is further demonstrated by the drastic change of the sensitivity of the plasmonic monolayers to the changes of refractive index. The bulk sensitivity of samples of different nanodisk density was tested by carrying out real-time and in-flow reflectivity measurements, thereby varying the bulk dielectric surrounding of the nanodisks (ΔRI = 0.02). Figure 5a shows that below the critical angle the experimental sensitivity (150 nm RIU^{-1}) is comparable

to that of similar nanodisk arrays on glass.[31,32] As a direct result of the interaction of the nanodisks with the high RI glass substrate, this value is substantially smaller than the theoretical values of a nanoellipsoid totally surrounded by water.[33] Interestingly, the sensitivity in TIR ($\theta = 80°$) for TM polarized light is similar to the one corresponding to low angle TE measurements (Figure 5a), which underlines the localized behavior for this polarization and the impossibility to excite guided modes. In contrast, Figure 5a shows that once the modal dispersion regime is launched in TIR for TE polarization, a steep rise of η_B is measured, increasing for larger incidence angles, with an overall larger enhancement for higher disk occupancies. Strongly influenced by the mode propagation at high incidence angles, it becomes thus possible to experimentally achieve an exceptional 4-fold increase of η_B for the high disk density substrate. The real-time measurement traces of both nanodisk samples, corresponding to their highest measured bulk sensitivity ($\theta = 85°$), are depicted in Figure 5b, thereby unambiguously illustrating this strong enhancement of the sensing performance. Consequently, these guided modes in random arrays of gold nanodisks profile themselves as very promising sensing platforms for real label-free biosensing applications.

On the other hand, even more important than the amplification of the sensitivity, the transition from weak reflectivity peaks below the critical angle into extremely profound dips in TIR can provide outstanding enhancements of the signal-to-noise ratio of the biosensing measurements. To illustrate this capability of the guiding modes we selected a low density nanodisk monolayer (5−6%) and we carried out a biosensing immunoassay, based on the specific detection of monoclonal antibodies previously produced against carbaryl (Carb),[34−36] a relevant and widely used pesticide. For these experiments, simultaneous monitoring of the real-time spectral displacements of the reflectivity spectra are performed at two different excitation angles ($\theta = 20°$ and $\theta = 75°$) using the same white light illumination intensity and identical acquisition conditions (exposure time 3 ms and 300 spectral accumulations). On the basis of previously discussed results, $\theta = 20°$ corresponds to a regime dictated by the LSPR of the nanodisks, while effective excitation of a guided mode is guaranteed at $\theta = 75°$. To create a self-assembled biological receptor layer for the specific detection of the antibody (anti-Carb), a five-step covalent immobilization protocol was carried out, whose corresponding real-time tracking of the resonance shift ($\Delta\lambda_{LSPR}$) is shown in Figure 5c. As can be observed, $\Delta\lambda_{LSPR}$ is approximately 50% larger in TIR, which fits the expected enhancement of the sensitivity at that nanodisk concentration and illumination angle (Figure 5a), proving the improved sensing performance of the guided modes. However, next to the larger absolute
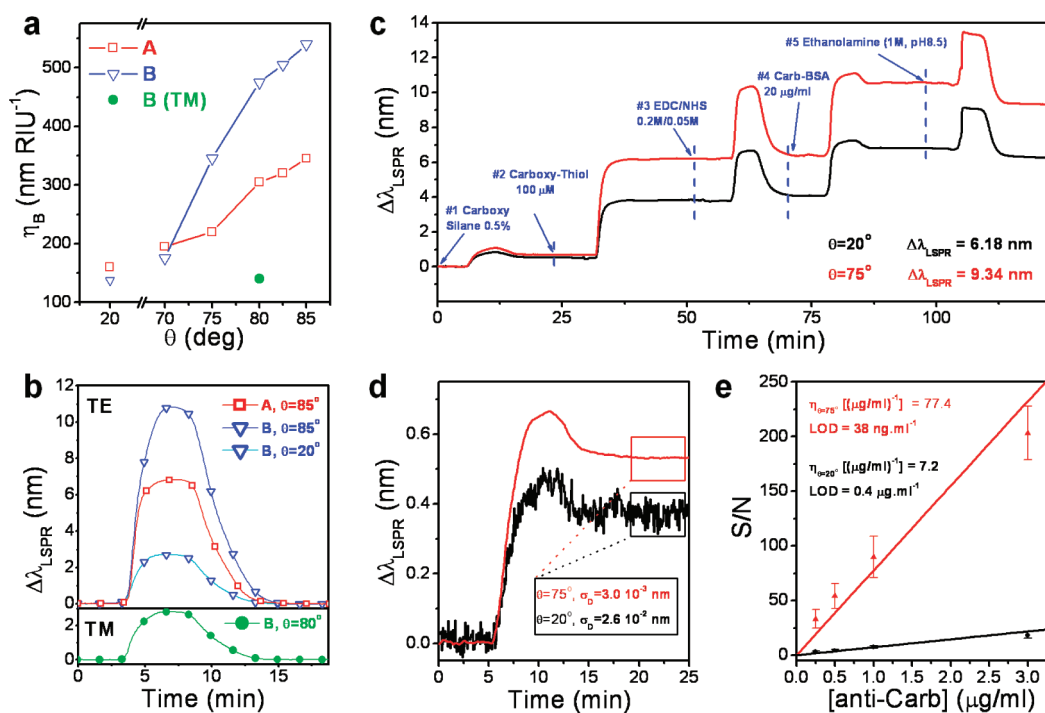
Figure 5. Experimental results involving label-free bulk- and biosensing features. (a) Angle-dependent TE and TM bulk sensitivities η_B of nanodisk arrays with disk densities given by $F \approx 5\%$ (A) and $F \approx 7.5\%$ (B). (b) Tracking of the spectral resonance shifts $\Delta\lambda_{LSPR}$ for samples A ($\theta = 85°$) and B ($\theta = 20°$, $\theta = 85°$, $\theta = 80°$/TM) as a function of time. (c) Real-time simultaneous tracking ($\theta = 20°$ and $\theta = 80°$) of the spectral resonance shift $\Delta\lambda_{LSPR}$ corresponding to the five-step immobilization protocol of Carb-BSA. (d) Detection curves of anti-Carb [3 μg/mL] at $\theta = 20°$ and $\theta = 80°$, showing the time-dependent resonance shift $\Delta\lambda_{LSPR}$. (e) Calibration curve of the anti-Carb detection assay, depicting the signal-to-noise ratio S/N as a function of the antiCarb concentration.

resonance shifts measured at $\theta = 75°$, this signal exhibits a noise level as low as 3 pm, despite of an acquisition performed with a low cost portable CCD spectrophotometer at room temperature with short integration time (<1 s), and the employment of only one-third of the pixels in the tracking algorithm. In Figure 5d, where simultaneous immunodetection signals of anti-Carb (3 μg/mL) at $\theta = 20°$ and $\theta = 75°$ are depicted, such dramatic noise suppression becomes apparent, showing a noise level difference of more than 1 order of magnitude between both measurement angles. This strong noise decrease is caused by the larger absolute signals of the resonance dips when perfect phase matching is achieved. Despite the almost perfect absorption band in the TIR configuration, the total amount of photons used in the tracking algorithm is 30-fold larger than below the critical angle. Since the noise level sets a limit to the discrimination of the smallest possible wavelength shift, the signal-to-noise ratio (S/N) is the desired variable to characterize the sensing performance of these nanoplasmonic structures. Following this path, and exploiting the regeneration potential of the immobilized biological receptor layer, detection of anti-Carb was carried out for a range of different concentrations (0.25–3 μg/mL). The obtained calibration curve, depicting S/N as a function of the antibody concentration (Figure 5e) exhibits a larger slope, and hence, an improved sensing compared to the

value obtained for $\theta = 20°$, that is 7.2 (μg/mL)$^{-1}$, results in an exceptional S/N enhancement of 1 order of magnitude. A corresponding limit of detection (LOD), defined as three times the noise level, as low as 38 ng/mL can be achieved. The response of this system thus shows the great potential that the guided modes in these sparse arrays of gold nanodisks have as biosensing platforms.

DISCUSSION

The novel waveguiding mechanism presented in this work is not restricted to gold nanodisks and can be applied to any sparse and random distribution of plasmonic nanoparticles, such as nanoprisms, nanorods, or core–shell nanostructures. Their inherent higher bulk sensitivity compared to nanodisks, allows expecting unprecedented sensitivities when the guided mode is launched. In addition, the waveguiding concept based on monolayers of plasmonic meta-atoms could also be expanded to achieve more exotic nanophotonic features with the introduction of plasmonic meta-molecules, such as interacting plasmonic dimers[31,37] or nanosandwiches.[38,39] These hybrid systems could combine the generation of additional effective birefringence effects, the creation of hot-spots or dark modes within the meta-molecules, with the excitation of the guided mode to amplify light/matter interaction, thus opening the path to envisage novel nanophotonic applications in light harvesting,

biosensing, or enhanced light emission/detection. Finally, it is worth noticing that the propagation distance of the analyzed guided modes can be substantially enhanced in a homogeneous configuration with a similar refractive index in substrate and cladding layers. In this configuration propagation distances larger than one millimeter are expected even for very low concentration nanoparticles for wavelengths in the NIR (Supporting Information, Figure S6), thus enabling integrated-optics applications.

METHODS

Simulations. Optical properties of the sparse arrays of nanodisks were calculated using the Maxwell−Garnett effective medium approximation, modeling the nanodisks as infinitely small oblate spheroids (aspect ratio = 5:1) embedded in a homogeneous dielectric ($n = 1.33$) using different disk densities ($F = 2-10\%$).[40] Optical constants of gold reported by Johnson and Christy were used.[41] For the angle- and polarization-dependent reflectivity spectra a transfer matrix formalism was employed, comprising the effective medium ($D = 20$ nm) between two cladding layers (glass, $n = 1.52$ and water, $n = 1.33$).[25] Bulk sensitivities were determined by inducing a RI change of $\Delta n = 0.005$ with respect to the RI of water ($n = 1.33$). Dispersion relation and mode propagation distances were calculated *via* an analytical formalism to determine the waveguiding properties of planar anisotropic multilayers.[22,23]

Fabrication. Sparse arrays of gold nanodisks ($D = 100$ nm, $H = 20$ nm (Ti/Au = 1/19 nm)) were fabricated on glass substrates (Menzel-Gläser, nr.4) *via* hole-mask colloidal lithography. To vary the disk occupancy, prior to the drop-coating of polysterene beads ($D = 100$ nm, W/V = 0.2%, Invitrogen), a diallyldimethylammonium chloride (7 kD, Sigma-Aldrich) layer with V/V ratios ranging from 1.5% to 3% was deposited on top of a poly(diallyldimethylammonium chloride) (200 kD, V/V = 2%, Sigma-Aldrich) and poly(sodium 4-styrene sulfonate) (70 kD, V/V = 2%, Sigma-Aldrich) bilayer. Before use, all samples were cleaned by consecutive 1-min sonication cycles in acetone, ethanol, and deionized water (2×) and dried under a constant flow of N_2. The samples were then placed in an ozone generator for 20 min, followed by thorough rinsing with deionized water, and then dried with N_2.

Measurements. Reflectivity spectra were obtained by exciting the nanostructures with a collimated halogen light source (HL-2000, Micropack) with TE or TM polarization, reaching the substrate *via* a hemicylindrical glass prism (K9, $n \approx 1.512$), contacting the sample *via* refractive index matching oil (Nikon, $n \approx 1.515$). Nanodisk substrates were comprised between the prism and a custom-made flow cell (Delrin, volume ≈ 4 μL). Both incident and reflected optical paths were mounted on arms rotating around the center point of the flow cell, guaranteeing the ability to carry out angle-dependent analyses. The reflected light was collected and fiber-coupled to a CCD spectrometer (Ocean Optics, Spectrasuite Jaz Module). Reflectivity spectra were acquired every 3 ms, with a total integration time of 900 ms (300 spectral accumulations). All spectra were normalized with a broad-band reference spectrum, obtained in TIR using the same acquisition settings. Tracking of the real-time resonance peak position was achieved *via* a high-degree polynomial fit, using the commercially available Wolfram Mathematica software package. Bulk sensitivity measurements were carried out by injecting a 12.8% glycerol solution ($n = 1.3525$) and extracting the induced spectral shift with respect to water ($n = 1.3325$). All presented values of η_B are averages over two separate measurements.

Surface Functionalization and Biosensing Measurements. A clean gold nanodisk surface was biofunctionalized under a constant flow of deionized H_2O at 20 μL/min. Both glass and gold were modified with carboxylic groups by injecting a 0.5% solution of carboxyethylsilanetriol sodium salt (CTES, Gelest LTd., UK) in distilled water followed by a solution of a carboxy- and thiol-terminated compound that contains four units of ethylene glycol (PEG) (CO_2H-EG-SH, 100 μM in 5 mM carbonate buffer). A derivative of the pesticide carbaryl conjugated to a carrier protein (Carb-BSA) was covalently attached to the carboxylic groups by means of the well-known carbodiimide reaction. First a mixture of 1-ethyl-3(-3 dimethylamino-propyl) carbodiimide hydrochloride (EDC) and N-hydroxysuccinimide (NHS), EDC/NHS (0.2 M/0.05 M in MES buffer) was injected in order to activate the carboxylic groups, followed by Carb-BSA (20 μg/mL in PBS) allowing for the free amino groups present in the conjugate to react. All remaining unreacted NHS-activated esters were deactivated by blocking the modified surface with ethanolamine (1 M, pH 8.5). Detection of specific antibody against carbaryl (monoclonal antibody Anticarb) at different concentrations (0.25−3 μg/mL) was carried out using PBS as interaction buffer. Regeneration of the bioactive surface was achieved by injecting a basic 100 mM NaOH solution for 30 s.

REFERENCES AND NOTES

1. Alaverdyan, Y.; Sepulveda, B.; Eurenius, L.; Olsson, E.; Kall, M. Optical Antennas Based on Coupled Nanoholes in Thin Metal Films. *Nat. Phys.* **2007**, *3*, 884–889.

2. Rindzevicius, T.; Alaverdyan, Y.; Sepulveda, B.; Pakizeh, T.; Käll, M.; Hillenbrand, R.; Aizpurua, J.; García de Abajo, F. J. Nanohole Plasmons in Optically Thin Gold Films. *J. Phys. Chem. C* **2006**, *111*, 1207–1212.

3. Charbonneau, R.; Berini, P.; Berolo, E.; Lisicka-Shrzek, E. Experimental Observation of Plasmon Polariton Waves Supported by a Thin Metal Film of Finite Width. *Opt. Lett.* **2000**, *25*, 844–846.

4. Salakhutdinov, I.; Thakur, J. S.; Leosson, K. Characterization of Long-Range Surface Plasmon-Polariton in Stripe Waveguides Using Scanning Near-Field Optical Microscopy. *J. Appl. Phys.* **2007**, *102*, 123110–123115.

5. De Leon, I.; Berini, P. Amplification of Long-Range Surface Plasmons by a Dipolar Gain Medium. *Nat. Photon.* **2010**, *4*, 382–387.

6. Verhagen, E.; Dionne, J. A.; Kuipers, L.; Atwater, H. A.; Polman, A. Near-Field Visualization of Strongly Confined Surface Plasmon Polaritons in Metal−Insulator−Metal Waveguides. *Nano Lett.* **2008**, *8*, 2925–2929.

7. Oulton, R. F.; Sorger, V. J.; Genov, D. A.; Pile, D. F. P.; Zhang, X. A Hybrid Plasmonic Waveguide for Subwavelength Confinement and Long-Range Propagation. *Nat. Photon.* **2008**, *2*, 496–500.

8. Sorger, V. J.; Ye, Z.; Oulton, R. F.; Wang, Y.; Bartal, G.; Yin, X.; Zhang, X. Experimental Demonstration of Low-Loss Optical Waveguiding at Deep Sub-wavelength Scales. *Nat. Commun.* **2011**, *2*, 331.

9. Bozhevolnyi, S. I.; Volkov, V. S.; Devaux, E.; Laluet, J.-Y.; Ebbesen, T. W. Channel Plasmon Subwavelength Waveguide Components Including Interferometers and Ring Resonators. *Nature* **2006**, *440*, 508–511.

10. Maier, S. A.; Kik, P. G.; Atwater, H. A.; Meltzer, S.; Harel, E.; Koel, B. E.; Requicha, A. A. G. Local Detection of Electromagnetic Energy Transport Below the Diffraction Limit in Metal Nanoparticle Plasmon Waveguides. *Nat. Mater.* **2003**, *2*, 229–232.

11. Auguié, B.; Barnes, W. L. Collective Resonances in Gold Nanoparticle Arrays. *Phys. Rev. Lett.* **2008**, *101*, 143902.

12. Chu, Y.; Schonbrun, E.; Yang, T.; Crozier, K. B. Experimental Observation of Narrow Surface Plasmon Resonances in Gold Nanoparticle Arrays. *Appl. Phys. Lett.* **2008**, *93*, 181108–181103.

13. Hicks, E. M.; Zou, S.; Schatz, G. C.; Spears, K. G.; Van Duyne, R. P.; Gunnarsson, L.; Rindzevicius, T.; Kasemo, B.; Käll, M. Controlling Plasmon Line Shapes through Diffractive Coupling in Linear Arrays of Cylindrical Nanoparticles Fabricated by Electron Beam Lithography. *Nano Lett.* **2005**, *5*, 1065–1070.

14. Kabashin, A. V.; Evans, P.; Pastkovsky, S.; Hendren, W.; Wurtz, G. A.; Atkinson, R.; Pollard, R.; Podolskiy, V. A.; Zayats, A. V. Plasmonic Nanorod Metamaterials for Biosensing. *Nat. Mater.* **2009**, *8*, 867–871.

15. Kravets, V. G.; Schedin, F.; Grigorenko, A. N. Extremely Narrow Plasmon Resonances Based on Diffraction Coupling of Localized Plasmons in Arrays of Metallic Nanoparticles. *Phys. Rev. Lett.* **2008**, *101*, 087403.

16. Vecchi, G.; Giannini, V.; Gómez Rivas, J. Surface Modes in Plasmonic Crystals Induced by Diffractive Coupling of Nanoantennas. *Phys. Rev. B* **2009**, *80*, 201401.

17. Yang, T.; Crozier, K. B. Dispersion and Extinction of Surface Plasmons in an Array of Gold Nanoparticle Chains: Influence of the Air/Glass Interface. *Opt. Exp.* **2008**, *16*, 8570–8580.

18. Zhou, W.; Odom, T. W. Tunable Subradiant Lattice Plasmons by Out-of-Plane Dipolar Interactions. *Nat. Nanotechnol.* **2011**, *6*, 423–427.

19. Fredriksson, H.; Alaverdyan, Y.; Dmitriev, A.; Langhammer, C.; Sutherland, D. S.; Zäch, M.; Kasemo, B. Hole-Mask Colloidal Lithography. *Adv. Mater.* **2007**, *19*, 4297–4302.

20. Holloway, C. L.; Kuester, E. F.; Novotny, D. Waveguides Composed of Metafilms/Metasurfaces: The Two-Dimensional Equivalent of Metamaterials. *IEEE Antennas Wireless Propag. Lett.* **2009**, *8*, 525–529.

21. Dong, J.-W.; Fung, K. H.; Chan, C. T.; Wang, H.-Z. Localization Characteristics of Two-Dimensional Quasicrystals Consisting of Metal Nanoparticles. *Phys. Rev. B* **2009**, *80*, 155118.

22. Sepúlveda, B.; Lechuga, L. M.; Armelles, G. Magnetooptic Effects in Surface-Plasmon-Polaritons Slab Waveguides. *J. Lightwave Technol.* **2006**, *24*, 945.

23. Vassell, M. O. Structure of Optical Guided Modes in Planar Multilayers of Optically Anisotropic Materials. *J. Opt. Soc. Am.* **1974**, *64*, 166–173.

24. Kretschmann, E. Die Bestimmung Optischer Konstanten Von Metallen Durch Anregung Von Oberflächenplasmaschwingungen (The Determination of Optical Constants of Metals by Excitation of Surface Plasma Oscillations). *Z. Phys. A: Hadrons Nuclei* **1971**, *241*, 313–324.

25. Schubert, M. Polarization-Dependent Optical Parameters of Arbitrarily Anisotropic Homogeneous Layered Systems. *Phys. Rev. B* **1996**, *53*, 4265–4265.

26. Homola, J. Surface Plasmon Resonance Sensors for Detection of Chemical and Biological Species. *Chem. Rev.* **2008**, *108*, 462–493.

27. Aubry, A.; Lei, D. Y.; Fernández-Domínguez, A. I. Sonnefraud, Y.; Maier, S. A.; Pendry, J. B. Plasmonic Light-Harvesting Devices over the Whole Visible Spectrum. *Nano Lett.* **2010**, *10*, 2574–2579.

28. Mayer, K. M.; Hafner, J. H. Localized Surface Plasmon Resonance Sensors. *Chem. Rev.* **2011**, *111*, 3828–3857.

29. Sepúlveda, B.; Angelomé, P. C.; Lechuga, L. M.; Liz-Marzán, L. M. LSPR-Based Nanobiosensors. *Nano Today* **2009**, *4*, 244–251.

30. Anker, J. N.; Hall, W. P.; Lyandres, O.; Shah, N. C.; Zhao, J.; Van Duyne, R. P. Biosensing with Plasmonic Nanosensors. *Nat. Mater.* **2008**, *7*, 442–453.

31. Otte, M. A.; Estévez, M. C.; Carrascosa, L. G.; González-Guerrero, A. B.; Lechuga, L. M.; Sepúlveda, B. Improved Biosensing Capability with Novel Suspended Nanodisks. *J. Phys. Chem. C* **2011**, *115*, 5344–5351.

32. Svedendahl, M.; Chen, S.; Dmitriev, A.; Käll, M. Refractometric Sensing Using Propagating *versus* Localized Surface Plasmons: A Direct Comparison. *Nano Lett.* **2009**, *9*, 4428–4433.

33. Otte, M. A.; Sepúlveda, B.; Ni, W.; Juste, J. P.; Liz-Marzán, L. M.; Lechuga, L. M. Identification of the Optimal Spectral Region for Plasmonic and Nanoplasmonic Sensing. *ACS Nano* **2010**, *4*, 349–357.

34. Abad, A.; Primo, J.; Montoya, A. Development of an Enzyme-Linked Immunosorbent Assay to Carbaryl. 1. Antibody Production from Several Haptens and Characterization in Different Immunoassay Formats. *J. Agric. Food Chem.* **1997**, *45*, 1486–1494.

35. González-Martínez, M. A.; Morais, S.; Puchades, R.; Maquieira, A.; Abad, A.; Montoya, A. Monoclonal Antibody-Based Flow-through Immunosensor for Analysis of Carbaryl. *Anal. Chem.* **1997**, *69*, 2812–2818.

36. Mauriz, E.; Calle, A.; Montoya, A.; Lechuga, L. M. Determination of Environmental Organic Pollutants with a Portable Optical Immunosensor. *Talanta* **2006**, *69*, 359–364.

37. Aćimović, S. S.; Kreuzer, M. P.; González, M. U.; Quidant, R. Plasmon Near-Field Coupling in Metal Dimers as a Step toward Single-Molecule Sensing. *ACS Nano* **2009**, *3*, 1231–1237.

38. Dmitriev, A.; Pakizeh, T.; Käll, M.; Sutherland, D. S. Gold−Silica−Gold Nanosandwiches: Tunable Bimodal Plasmonic Resonators. *Small* **2007**, *3*, 294–299.

39. González-Díaz, J. B.; García-Martín, A.; García-Martín, J. M.; Cebollada, A.; Armelles, G.; Sepúlveda, B.; Alaverdyan, Y.; Käll, M. Plasmonic Au/Co/Au Nanosandwiches with Enhanced Magneto-optical Activity. *Small* **2008**, *4*, 202–205.

40. Sihvola, A. H.; Kong, J. A. Effective Permittivity of Dielectric Mixtures. *IEEE Trans. Geosci. Remote Sensing* **1988**, *26*, 420–429.

41. Johnson, P. B.; Christy, R. W. Optical Constants of the Noble Metals. *Phys. Rev. B* **1972**, *6*, 4370–4379.